NANO · MICRO small
www.small-journal.com

Atomic Basal Defect-Rich MoS_2 by One-Step Synthesis and Mechanism Exploration

Haowen He, FengXue Tan, YingJiao Zhai, FuJun Liu,* DengKui Wang, Xuan Fang, Jinhua Li, and Sophie Laurent**

Two-dimensional molybdenum disulfide (2D MoS_2) shows great promise as a surface-enhanced Raman scattering (SERS) substrate due to its strong exciton resonance. However, the inert basal plane limits the performance of SERS. In this work, a strategy is proposed for the one-step synthesis of atomically basal defect-rich MoS_2. The study first reveals that NaCl plays a two-stage role in the growth process, where NaCl initially promotes the rapid growth of large MoS_2 as previously reported, and then promotes the formation of atomic basal defects dominated by single sulfur vacancies. Additionally, spectral changes induced by modulation of experimental parameters and density function theory calculation show that defect generation occurs during cooling. Meanwhile, the ratio of E^1_{2g} to A_{1g} in defect-rich MoS_2 exhibits different variation trends compared with pristine MoS_2 in power-dependent Raman, and the ratio increases with increasing basal defects. In SERS tests, the limit of detection for rhodamine 6G reached 10^{-9} M, which is comparable to the performance of conventional noble metal SERS substrate. The activation strategy of the inert basal plane is applicable to other 2D transition metal dichalcogenides, and further has the potential to enhance performance in other domains, such as SERS and hydrogen evolution reactions.

1. Introduction

In recent years, 2D transition metal dichalcogenide(2D TMD) materials have attracted broad attention in the surface-enhanced Raman scattering (SERS) domain due to their strong excitonic resonance.[1–3] Monolayer MoS_2 has been proven to have excellent SERS performance.[4] The A exciton bandgap, ≈1.85eV,[5] facillitates MoS_2 triggering exciton resonance in visible light, and electrons can more easily transfer from MoS_2 to probe molecules than those in bilayer or multilayer structures.[6] However, the poor dangling bonds on the basal plane cannot supply sufficient active sites, and the inert basal plane hinders the improvement of SERS ability. Thus the introduction of basal defects shows more significance in enhancing 2D semiconductor substrates.[7–9]

Rational defect engineering not only improves the absorption efficiency of analyte, but also accelerates charge transfer(CT) and photoinduced charge transfer(PICT) processes between MoS_2 and molecules.[10] To activate the inert basal plane of MoS_2, current strategies can be divided into two categories: physical and chemical methods.[11–14] The former commonly use chemical reducing agents to treat MoS_2. For example, using $NaBH_4$ allows S atoms to react with H cations to induce basal defect formation.[15] This effectively increases the number of active sites but inevitably causes a solvent residue problem, and the treatment is mostly applicable to few-layer MoS_2. Physical strategies can avoid these problems. For instance, utilizing laser or plasmon irradiation of the surface can destroy the lattice structure to induce sulfur vacancies,[16–18] but this usually leads to a collective loss of atoms in the irradiated region and is unable to form atomic basal defects. High-temperature annealing can also induce defects but can not guarantee uniformity.[19] The abovementioned strategies are all based on the prepared MoS_2 with secondary treatment for basal plane activation. This two-step strategy is not only tedious in operation but also inevitably results in interfacial contamination that reduces the performance. Additionally, the introduction of atomic basal defects can guarantee spatial uniformity and structural homogeneity,[20] which is conducive to performance enhancement and stability. Therefore, it is vital to activate the inert plane of MoS_2 in one step by introducing atomic basal defects.

H. He, F. Tan, Y. Zhai, F. Liu, J. Li
Ministry of Education Key Laboratory for Cross-Scale Micro and Nano Manufacturing
Nanophotonics and Biophotonics Key Laboratory of Jilin Province
Changchun University of Science and Technology
Changchun 130022, P. R. China
E-mail: yjzhai@cust.edu.cn; fjliu@cust.edu.cn

D. Wang, X. Fang
State Key Laboratory of High Power Semiconductor Lasers
School of Physics
ChangchunUniversity of Science and Technology
7089 Wei-Xing Road, Changchun 130022, P. R. China

S. Laurent
NMR and Molecular Imaging Laboratory
Department of General
Organic and Biomedical Chemistry
University of Mons
19 Avenue Maistriau, Mons 7000, Belgium
E-mail: sophie.laurent@umons.ac.be

S. Laurent
BelgiumCenter for Microscopy and Molecular Imaging (CMMI)
8 Rue Adrienne Boland, Gosselies 6041, Belgium

The ORCID identification number(s) for the author(s) of this article can be found under https://doi.org/10.1002/smll.202404684

DOI: 10.1002/smll.202404684

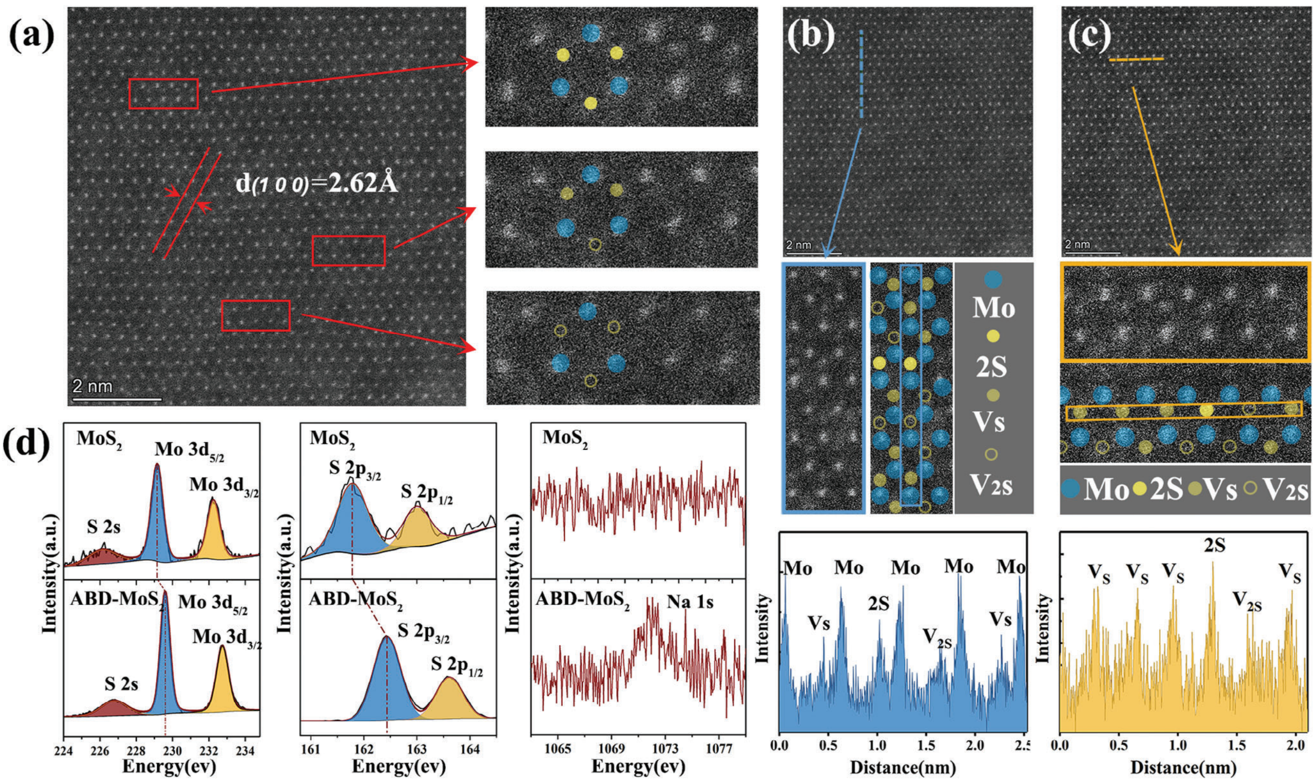

Figure 1. a) HAADF-STEM characterization of ABD-MoS_2 and the distance of < 100 > is 2.60 Å, the three images on the right side show zoomed-in images of different brightness regions, the atomic arrangement along with armchair b) and S-zz c) edge with HAADF intensity profile images, d) XPS spectra of Mo3d, S2p, Na1s in MoS_2 and ABD-MoS_2.

In this work, we propose a one-step strategy to obtain MoS_2 with atomic basal plane defects(ABD-MoS_2). High-angle annular dark field scanning transmission electron microscopy(HAADF-STEM) is used to study the type and uniformity of the introduced basal defects. By analyzing the spectral changes under different reaction parameters, and combining them with theoretical calculations, we reveal the mechanism of surface defect formation using NaCl. The strategy also provides a new approach for activating the basal plane of other 2D TMD materials. It also provides a new method for application in SERS domain.

2. Results and Discussion

2.1. The Characterization of ABD-MoS_2

HAADF-STEM and X-ray photoelectron spectroscopy (XPS) revealed many alternating light and dark areas on the surface ofABD-MoS_2 (**Figure** 1a). In the HAADF-STEM image, regions with higher atomic number (Z) scatter more electrons and appear brighter. Therefore, the Mo atom ($Z = 42$) appears the brightest followed by double sulfur atoms (2S), single sulfur vacancy (V_S), and double sulfur vacancy (V_{2S}). By zooming in on the three regions with different brightness in Figure 1a (indicated by red boxes), it becomes evident that the bright region contains visible S and Mo atoms, the darker region shows decreased brightness due to the presence of the V_S, and the darkest region displays only Mo atoms. The blue spheres represent Mo atoms, the yellow spheres represent 2S, the light yellow spheres represent V_S, and the light yellow circles represent V_{2S}. Consequently, the surface contains a significant number of Vsand V_{2S}. Figure 1b,c shows magnified images of selected regions in ABD-MoS_2 along the armchair and S-zigzag(S-zz) orientation, respectively, along with the HAADF intensity profile. In this profile, the ratio of S atom intensity to Mo atom intensity indicates that the 2S intensity ratio is ≈0.77, while the V_S intensity decreases to 0.65, and the V_{2S} intensity ratio decreases to ≈0.57. Furthermore, V_S is the predominant type of defect and is abundantly present on the surface of ABD-MoS_2 substrate.

We performed further analysis using XPS. Figure 1d shows the XPS spectra of the Mo3d, S2p and Na1s core-level emissions for the MoS_2 sample and ABD-MoS_2. The Mo3d of MoS_2 can be fitted into three characteristic peaks at 226.19 (S2s), 229.14 ($Mo3d_{5/2}$), and 232.19 eV ($Mo3d_{3/2}$). The characteristic doublet of S2p can be fitted into two peaks at 161.79 ($S2p_{3/2}$) and 162.99 eV ($S2p_{1/2}$).[21] The position of $Mo3d_{5/2}$in ABD-MoS_2 shifted 0.38 eV toward a higher binding energy, and $S2p_{3/2}$ also exhibits the same phenomenon, which is commonly related to defect formation.[22] By utilizing the corresponding sensitivity factor and the integral intensity of Mo $3d_{5/2}$ and S $2p_{3/2}$, we obtained the stoichiometric ratios of S and Mo for MoS_2 and ABD-MoS_2 after calculation (the calculation is detailed in Equation S1, Supporting Information). The result shows that $MoS_{1.99}$ transforms to $MoS_{1.89}$, and

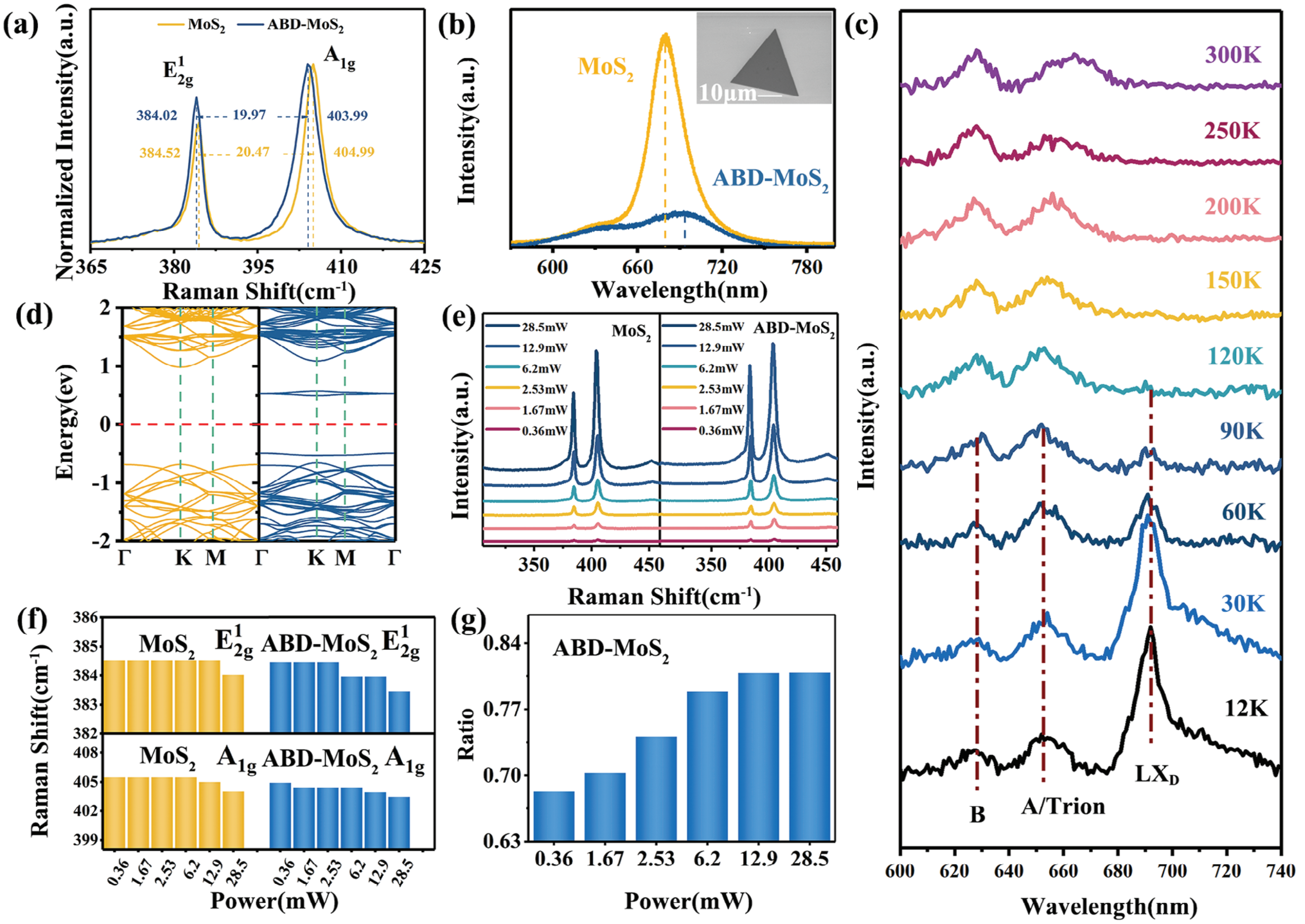

Figure 2. Comparison of Raman (a) and PL (b) of MoS_2 and ABD-MoS_2, the insert image is SEM image of ABD-MoS_2 (c) the temperature-dependent PL spectra of ABD-MoS_2 (d) the band structure of 4×4 supercell MoS_2 with and without S vacancy on the surface. e) Raman spectra of MoS_2 and ABD-MoS_2 with different laser power. Comparison of the intensity (f) the position of E^1_{2g} and A_{1g} modes of MoS_2 and ABD-MoS_2 with different laser power (g) the ratio of E^1_{2g} to A_{1g} of ABD-MoS_2 with different laser power.

the sulfur–sulfur distance is 3.08Å. Thus, $MoS_{1.89}$ with a defect concentration of 5.5% is equivalent to a sulfur vacancies density of $1.78 \times 10^{14} cm^{-2}$. Moreover, it is evident that the characteristic peak of Na is present only in ABD-MoS_2 but not in MoS_2, which provides evidence for the formation of basal sulfur vacancies under a Na atmosphere.

2.2. Laser Power-Dependent Characterization of ABD-MoS_2

The presence of a large number of basal defects inevitably affects the lattice stability and electronic properties of ABD-MoS_2.[23] The shift of the in-plane vibrational peak E^1_{2g} and the out-of-plane vibrational peak A_{1g} modes in the Raman spectra of MoS_2 can reflect changes in mechanical strain (ϵ) and electron doping (n). The E^1_{2g} mode is more affected by internal mechanical strain, while the A_{1g} mode is sensitive to electron doping due to strong coupling with electrons.[24] In ABD-MoS_2, SiO_2/Si substrate has a low lattice match with ABD-MoS_2, which induces tensile strain and electron doping, while laser irradiation and sulfur vacancies induce compressive strain and electron doping.[25,26] The synergistic effect of above three factors led to the shift of the E^1_{2g} and A_{1g} modes. After Raman characterization of the prepared ABD-MoS_2 and pristine MoS_2, **Figure 2a** shows the E^1_{2g} and the A_{1g} modes of ABD-MoS_2 (pristine MoS_2) located at $383.96 cm^{-1}$ ($384.52 cm^{-1}$) and $403.94 cm^{-1}$ ($404.99 cm^{-1}$), respectively.[27] The E^1_{2g} and A_{1g} modes of ABD-MoS_2 were red-shifted compared to pristine MoS_2, which is associated with the presence of defects,[28] and also proved that the sulfur vacancies induced compressive strain and electron doping. Figure 2b shows a significant fluorescence quenching in the photoluminescence (PL) spectra of ABD-MoS_2, with an obvious redshift in peak position. The inserted SEM image shows the size of ABD-MoS_2 to be ≈ 28.3 μm. This phenomenon indicated electron doping and the introduction of defect states. In addition, in the temperature-dependent PL spectra, bound exciton(LX_D) luminescence caused by exciton trapped at defect states was observed at 12K, which further proves the existence of basal defects (Figure 2c).[29] We used DFT to calculate the band structure of MoS_2 and MoS_2 with a single V_S. The result shows that the two defect state levels are introduced into the gap of MoS_2 after the introduction of sulfur vacancy. One is located at 0.5 eV below the conduction band and the other is located at 0.13 eV above the top of the valence band. The intrinsic transition energy decreased from 1.650 to 1.632 eV after $V_S$formation (Figure 2d).

Figure 2e shows the power-dependent Raman spectra of MoS_2 and ABD-MoS_2. The intensities of the two vibrational modes of MoS_2 and ABD-MoS_2 are enhanced as the laser power increases from 0.36 to 28.5 mW.Pristine MoS_2 has fewer basal defects, so the E^1_{2g} mode does not shift between 0.36 to 12.9 mW, only redshifted under 28.5 mW. On the other hand, electron doping caused by the increase of power makes the A_{1g} mode gradually shift. The A_{1g} mode is gradually enhanced due to increased electronic doping. While in ABD-MoS_2, the order of magnitude of defects is lower than 10^{15} cm^{-2}, so ABD-MoS_2 still maintains a better lattice arrangement between 0.36 to 2.53 mW without causing E^1_{2g} to shift.[30] The basal defect caused the E^1_{2g} mode to redshift under 6.2 mW, earlier than MoS_2. The A_{1g} mode also redshifted due to electron doping, but the basal defects make the redshift degree greater than that of MoS_2 under the same power(Figure 2f). By calculating the mechanical strain and electron doping of MoS_2 and ABD-MoS_2under 28.5 mW compared to MoS_2 under 0.36 mW, it is obtained that $\epsilon(MoS_2)$ is 0.628% and $n(MoS_2)$ is 1.91×10^{12} cm^{-2}, while ϵ(ABD-MoS_2) is 0.793% and n(ABD-MoS_2) is 3.05×10^{12} cm^{-2}(the calculation details are provided in Equation S2, Supporting Information). The results show that the increase in laser power and the number of basal defects leads to compressive strain and electron doping, and the strain and doping degree of ABD-MoS_2 are the highest. Moreover, the ratio of E^1_{2g} to A_{1g} in ABD-MoS_2 increased with laser power(Figure 2g).

2.3. The Defect Formation Mechanism in ABD-MoS_2

The increase of defects on the basal plane often leads to changes in the properties of MoS_2. These defects will cause fluorescence quenching in MoS_2, resulting in a reduction in its luminescence intensity. In addition, the main peak of MoS_2's PL is typically attributed to the A exciton and charged exciton (also known as Trion). An increase in defects leads to more free electrons in the system, causing a transformation of A excitons to Trion.[31] This transformation is characterized by a red shift of the main PL peak. Therefore, the change in defects can be determined by observing the change in the normalized intensity of Trion in the PL peak of MoS_2.

To clarify the mechanism of basal defects formation, we first studied ABD-MoS_2 growth with different NaCl masses: 2.5, 7.5, 12.5, and 17.5 mg (denoted as Na_x-MoS_2, where x represents the mass of NaCl added). From the SEM images in **Figure 3**a, it is evident that the size of Na_x-MoS_2 increased becomes larger and the film shows a tendency toward bilayer growth with increasing NaCl mass. Raman characterization also shows that an increase in NaCl mass introduces a higher ratio, which reaches a maximum at 12.5 mg (Figure 3b). Figure 3c also demonstrates that the PL intensity decreased with the increase of NaCl mass, along with a gradual redshift. Our calculations, through building different supercells and removing one or two S atoms to simulate different Vs concentrations (Figure S1, Supporting Information), shows that an increase in Vs leads to a decreased bandgap and the generation ofmore defect states between the valence band and conduction band(Figure S2, Supporting Information). Therefore, the increase in basal defects will result in intensified fluorescence quenching, indicating that $Na_{12.5}$-MoS_2 has the highest number of defects. Moreover, the density states of different S vacancy concentrations demonstrate that both the conduction band and the valence band are provided with electrons by Mo $d_{x^2-y^2}$ orbital (Figures S3 and S4, Supporting Information).After analyzing the PL splitting peaks at different NaCl masses, it was found that the carriers introduced by basal defects shifted more A excitons toward Trion (Figure 3d). Furthermore, the trend of ratio change is consistent with the normalized intensity of Trion (Figure 3e), providing evidence for the use of Raman and PL to demonstrate changes in defect amounts in the basal plane. However, defects do not always increase with increasing NaCl mass (Figure 3f). When the mass of NaCl is up to 17.5 mg, the strength of PL increases, because excessive NaCl will activate the secondary growth of MoS_2, thus consume Na atoms in the atmosphere and reducing the number of base defects. In addition, $Na_{12.5}$-MoS_2 without and with secondary growth trends were characterized by HAADF-STEM(Figure 3g). The figure shows that the latter has significantly better crystallinity, with a uniform brightness distribution and fewer basal defects. We hypothesize that, this phenomenon arises from the fact that the formation of basal defects does not occur during growth. After Na atoms promote ABD-MoS_2 growth, the remaining atoms are adsorbed by basal sulfur atoms and prepared for defect generation. If ABD-MoS_2 activates the secondary growth, it will consume the number of absorbed Na atoms on the basal plane, which ultimately leads to the reduction of the defects.

To verify that after NaCl promotes growth in the first stage, the adsorbed Na atoms begin to induce basal defects in the second stage. We synthesized $Na_{12.5}$-MoS_2 at different reaction times (t_y-MoS_2, wheret_y represents the reaction time of y minites). SEM images show that t_{20}-MoS_2 has many jagged edges produced by incomplete contraction of Mo-zz and S-zz.[32] With the extension of time, the S-zz edge of t_{50}-MoS_2 continued to contract under the S-rich atmosphere, eventually forming a triangular monolayer t_{60}-MoS_2. Further extension of the reaction time led to the activation of the secondary growth of t_{80}-MoS_2 and the formation of cloud-like boundary (**Figure 4**a).[33] This can also be seen in the Raman and PL characterization. The ratio of t_{20}-MoS_2 was larger than t_{50}-MoS_2, possibly due to the incomplete contraction of the edge, and PL spectra performed similarly to pristine MoS_2 because Na atoms only played a role in assisting growth in the initial stage. When the reaction time further increased, the continued contraction of t_{50}-MoS_2 led to a decrease in the ratio, and Na atoms began to induce basal defect formation. t_{60}-MoS_2 showed the maximum quantity of defects, and the ratio of t_{80}-MoS_2 decreased due to secondary growth(Figure 4b). Meanwhile, the PL spectra of $t_{50,\ 60,80}$-MoS_2 did not show significant differences because the same mass of NaCl was added(Figure 4c). After fitting the split peaks of t_x-MoS_2($t = 20$, 50, 60, and 80), t_{60}-MoS_2 showed the maximum normalized intensity of Trion, indicating that the most defects existed on the basal plane after 60 min of reaction time(Figure 4d). Furthermore, secondary growth led to a decrease in the normalized intensity of trion in t_{80}-MoS_2. The trend of normalized intensity of Trion was consistent with the ratio of E^1_{2g} to

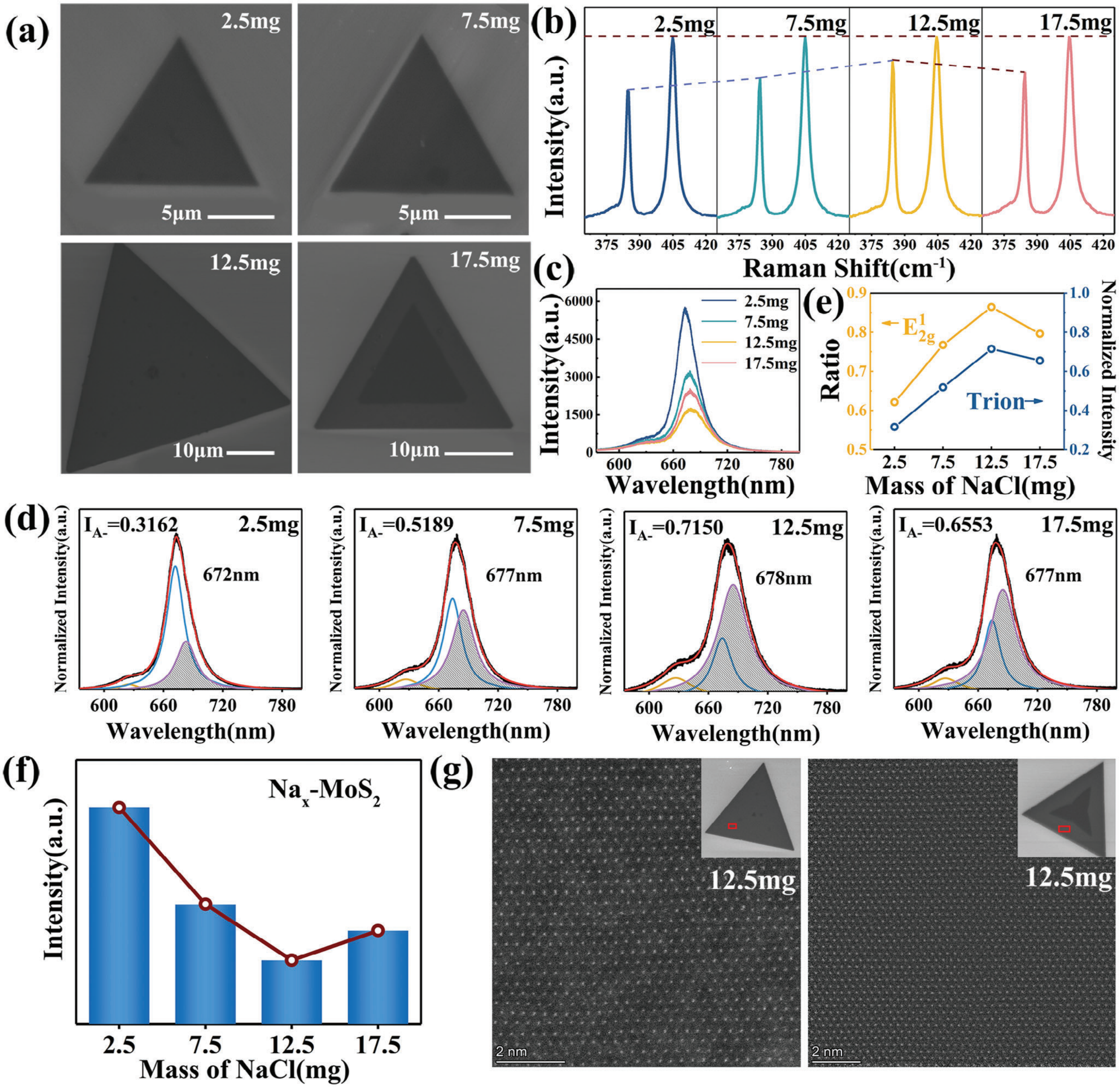

Figure 3. a) the SEM images of Na_x-MoS_2 (x = 2.5, 7.5, 12.5, and 17.5 mg), Raman(b), PL(c), and peak fitting(d) spectra of different NaCl mass Na_x-MoS_2, e) comparison of ratio and normalized intensity of Trion, (f) the PL peak intensity of Na_x-MoS_2 (Na_x represent added NaCl mass, x = 2.5, 7.5, 12.5 and 17.5 mg here), g) the HAADF-STEM images of monolayer region in full monolayer and bilayer $Na_{12.5}$-MoS_2.

A_{1g}, except for the difference in t_{20}-MoS_2 due to the incomplete contraction of the edge(Figure 4e). Therefore, basal defects can only be generated after MoS_2 growth(cooling).

DFT calculations showed that in the model of Na adsorbed on the basal sulfur atom(**Figure 5a**), the formation energy of Na-S adsorbed on ABD-MoS_2 with Vs gradually increased with decreasing temperature. On the other hand, the formation energy of Vs with Na atom adsorbed on the surface of ABD-MoS_2 gradually decreased(Figure 5b) and was lower than the formation energy without Na atom adsorbed on the surface of ABD-MoS_2. This proves that NaCl can decrease the formation energy of Vs and increase the concentration of Vs. When the temperature is higher than 1039K (776 °C, point B), the Na atom adsorbed on the surface is more stable than the formation energy of Vs. This proves that at high temperatures, the Na atom is adsorbed on the surface and contributes to the growth of ABD-MoS_2. When the temperature is lower than 800 K (526.4 °C, point A), the formation energy of Vs is negative, indicating that it can be formed spontaneously. This proves that during the cooling process, a large number of Vs are formed. Therefore, at the beginning of the

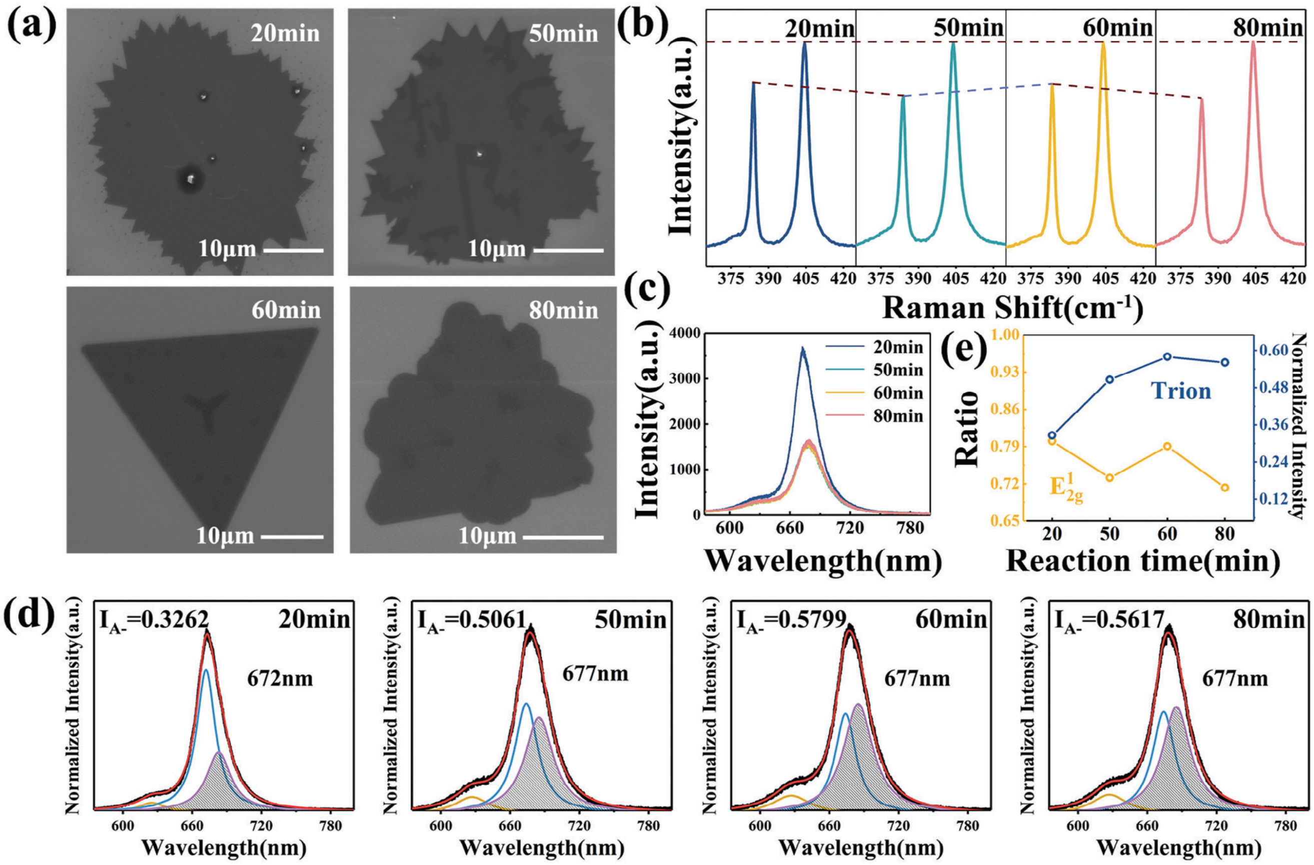

Figure 4. a) the SEM images of $Na_{12.5}$-MoS_2 in different reaction time, Raman(b), PL(c), and peak fitting(d) spectra of t_{20}-MoS_2, t_{50}-MoS_2, t_{60}-MoS_2, and t_{80}-MoS_2, e) comparison of ratio and normalized intensity of Trion.

cooling process, the adsorbed Na atoms on the surface of ABD-MoS_2 can induce the formation of atomic basal defects in large quantities. As the temperature continues to decrease, the formation energy of Vs with Na atoms becomes even lower, leading to the spontaneous generation of basal defects. Without NaCl, Vs can be formed spontaneously when the temperature is lower than 558 K(284 °C).

Based on the effect of adjusting NaCl mass and reaction time on the number of basal defects and DFT calculations, we determined the two stages role played by NaCl in the growth of MoS_2 as well as the specific mechanism of basal defect formation (Figure 5c). In the first stage at the beginning of the reaction, Na atoms began to adsorb on the edge of ABD-MoS_2 to promote edge contraction and achieve rapid growth. When the edge is about to finish contracting to a triangular transition, it enters the second stage. In this stage, many Na atoms began to adsorb on the surface of ABD-MoS_2, forming a Na-S-Mo system. Before the surface is saturated, Na in the atmosphere can continuously adsorb on the surface. When the adsorption is saturated, the reaction is still going or a large amount of Na still exists in the atmosphere, leading to secondary growth. This results in the formation of multilayer or cloudy edge ABD-MoS_2, consuming the Na atoms in the system. When the reaction is over, the defect formation stage begins. Due to the decreased temperature in the furnace, the energy of the Na-S-Mo system rises, causing a large number of basal S atoms to detach from the surface, and ultimately synthesize ABD-MoS_2. This mechanism of basal defects generation using adsorption-detachment of alkali metal atoms from basal sulfur atoms has been reported.[34] However, the difference is that the prepared ABD-MoS_2 in this work still formed a large number of basal defects in the absence of H_2O molecule, and we consider that Na atoms combined with basal sulfur atoms at high temperature, and the Na-S system spontaneously detached to form basal defects when the system during cooling.

2.4. The SERS Performance of ABD-MoS_2

In the previous discussion, we have outlined the mechanism of basal defect generation. It is widely known that the presence of defects can increase the number of active sites on the surface of MoS_2 and enhance the SERS performance. We compared the SERS performance of optimized MoS_2 with that of pristine MoS_2 at a concentration of 10^{-5} $_M$ rhodamine 6G(R6G), and the results indicate a significant improvement in SERS performance significantly with the activation of the basal plane (**Figure 6a**). Meanwhile, to confirm our conclusion, we conducted SERS detection on ABD-MoS_2 with varying masses of NaCl and reaction times. The results showed that the SERS performance was achieved with a NaCl mass of 12.5 mg, which resulted in the highest

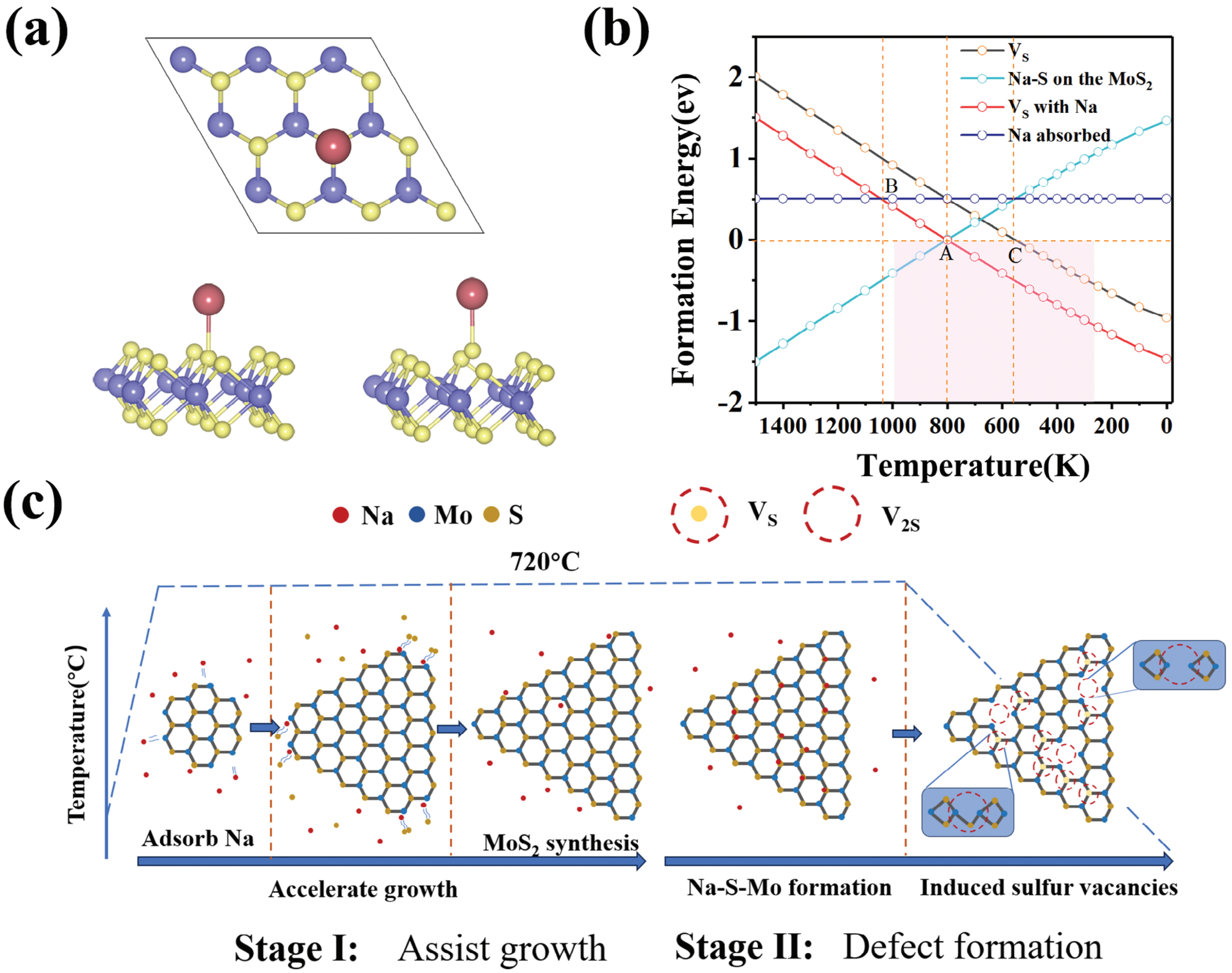

Figure 5. a) The model of the top view and side view of the Na atom absorbed on the surface of ABD-MoS_2, and the side view of the Na-S detachment from the surface of MoS_2, b) the formation energy of Vs in the condition of with and without NaCl with as a function of temperature c) the schematic illustration of the role of NaCl in ABD-MoS_2 growth.

number of defects on the basal plane (Figure 6b). Furthermore, the number of defects reached its maximum at 60 min of reaction time, but at 80 min, the absorbed Na atoms were consumed, resulting in a reduction in basal defects. This trend was also observed in the SERS performance (Figure 6c). Figure 6d displays the intensity trends of characteristic peaks at 613 cm^{-1}in 10^{-5} M R6G with different parameters of ABD-MoS_2. It is evident that the strategy successfully introduced basal defects in MoS_2 to effectively enhance the SERS performance.

In addition, we also modulated the mass of Mosource (Figure S5, Supporting Information), reaction temperature(Figure S6, Supporting Information), and carrier gas flow rate(Figure S7, Supporting Information). The results showed that as the mass of the Mo source increased, the number of basal defects decreased and the SERS performance decreased. This can be attributed to the higher Mo source, resulting in more ABD-MoS_2 generation and depletion of Na atoms in the atmosphere. On the other hand, an increase in temperature led to more Na atoms assisting in defect formation during cooling, thereby enhancing the SERS performance. Moreover, an increase in carrier gas flow rate gradually reduced the number of Na atoms adsorbed on the ABD-MoS_2 surface, leading to a decrease in the SERS performance.

To further investigate the mechanism for the SERS of ABD-MoS_2, we conducted the DFT calculations to reveal the charge transfer process between R6G and MoS_2 (Figure 6e). The electron localization function of the MoS_2 at the center, situated below the R6G molecule, is larger than that at the edge (Figure 6f). As a result, the R6G molecule receives electrons at the center, causing polarization and loss of electrons from the H atom. Furthermore, the visualized charge density redistribution shows that the charge transfers from R6G to MoS_2.enhancing the polarizability tensor of R6G molecule for improved SERS performance,[35] the SERS intesity (I) is shown in following the Equation (1):

$$I = [8\pi(\omega \pm \omega_{I'I})^4 I_L/9c^4]\Sigma\alpha_{\sigma\rho}^2 \tag{1}$$

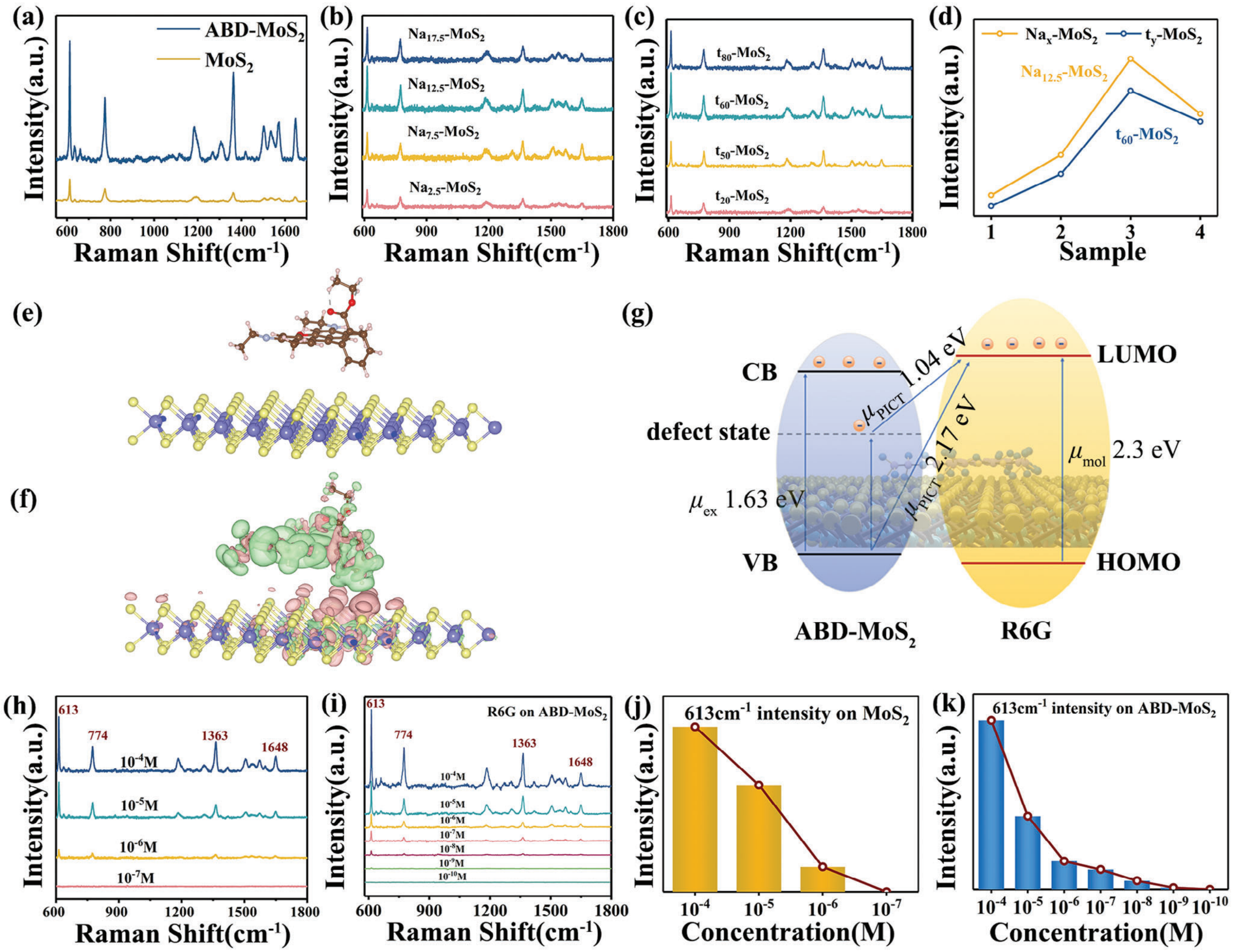

Figure 6. a) SERS performance comparison of MoS$_2$ and ABD-MoS$_2$ with 10^{-5} м R6G. b)The SERS performance in different NaCl mass and c) reaction time, d) the 613 cm^{-1} characteristic peak intensity of four samples with different parameters(Na$_x$-MoS$_2$, t_y-MoS$_2$) by using 10^{-5} м R6G, e) the R6G molecular absorbed on MoS$_2$ with one Vs on the surface, f) The Charge density difference of R6G molecular on MoS$_2$.The isosurface level is 0.00024, and the red and green areas are the electron accumulation and depletion regions, respectively, g) Schematic illustration of charge transfer mechanism between ABD-MoS$_2$ and R6G, h) the LOD test of MoS$_2$ and i) ABD-MoS$_2$, j) 613 cm^{-1} characteristic peak intensity in different concentration from 10^{-4} to 10^{-7} м, (k) 613 cm^{-1} characteristic peak intensity in different concentration from 10^{-4} to 10^{-10} м.

where ω and I_L is the incident laser angular frequency and intensity, $\omega_{I'I}$is a transition frequency between states I and I', c is the lightspeed and $\alpha_{\sigma\rho}$ is the polarizability tensor.

According to our calculations and previous reports,[1,36] the schematic of CT between ABD-MoS$_2$ and R6G is shown in Figure 6g. The PICT energy between the valence band(VB) of ABD-MoS$_2$ and the lowest unoccupied molecular orbital(LUMO) of R6G is2.17 eV, and the energy from the highest occupied molecular orbital to LUMO of the R6G molecule is2.3 eV, both close to the incident laser energy of 2.33 eV (532 nm). This results in a strong CT resonance in semiconductor-molecule systems and molecular resonance in R6G. In addition, due to the presence of defect state in ABD-MoS$_2$, the electrons in VB can leap into the defect state under the laser excitation, and then from the defect state to the LUMO. The defect states provide an additional CT path, promoting the radiative combination of free electrons and thus releasing more Raman photons. The synergistic effect of CT, resonance enhancement, and surface active sites introduced by a large number of basal defects enhances the SERS performance of ABD-MoS$_2$. Moreover, the limit of detection(LOD) of MoS$_2$ can reach 10^{-6} м, and ABD-MoS$_2$ can reach 10^{-9} м, which is comparable to noble metal substrates (Figure 6h–k).

3. Conclusion

In this work, we presented a two-stage action of NaCl in MoS$_2$. It is demonstrated that NaCl assists in the formation of atomic basal defects after the rapid growth of MoS$_2$. During the reaction process, Na atoms are adsorbed on the ABD-MoS$_2$ basal surface, causing the detachment of basal S atoms to form vacancies during the cooling process. By this way, the inert substrate surface of MoS$_2$ can be effectively activated to improve its SERS performance, enabling it to reach a LOD of 10^{-9}мfor detecting R6G.This not only enhanced semiconductor SERS performance to be comparable to metal substrate, but also provides a new strategy for the rest of the TMDs materials to conveniently introduce defects to enhance their performance.

4. Experimental Section

Preparation of ABD-MoS$_2$: ABD-MoS$_2$ was synthesized using chemical vapor deposition. In brief, sublimed sulfur powder(200 mg in the corundum boat) was placed in the first temperature zone of quartz furnace, and mixture of MoO$_3$(20 mg) and NaCl(12.5 mg)was placed in the second one. The wafer was cut into 1 cm^2-sized substrate and then sonicated with trichloroethylene(10 mL), acetone(10 mL), ethanol(10 mL), and deionized water(10 mL) for 15 min and blown dry, respectively. The cleaned substrate was placed upside-down on a corundum boat downstream of the mixing source near the front of the corundum boat. The entire experimental equipment is shown in Figure S8 (Supporting Information). 70sccm of the nitrogen for 1 h to exhaust the air inside before reaction start. During the reaction, both the low and high-temperature zones were raised to 165 and 720 °C with in1h and then the temperature was maintained for 1 h to grow ABD-MoS$_2$ under 30 sccm flow rate. When the reaction was finished, the sample was taken out after furnace was cooled down to room temperature. the ABD-MoS$_2$ preparation was completed.

Characterization: HAADF-STEM data were collected by Titan Cubed Themis G2 300 with 300kv. XPS spectral of MoS$_2$ and ABD-MoS$_2$ obtained by using Thermo Fisher ESCALAB XI$^+$ with 20kv. Raman and PL signal were measured through labRAM HR Evolution with 532 nm. The morphology of samples was collected by JEOL JSM-6010LA.

DFT Calculation: The density functional theory (DFT) calculations were carried out with the Vienna ab initio simulation package (VASP). with the electronic interaction being described by the Projector Augmented-Wave (PAW) potential, and Perdew, Burke, and Ernzerhof (PBE) form of the Generalized Gradient Approximation (GGA) is adopted for the exchange-correlation energy. The valence electrons for S and Mo were $3s^{2}$ $3p^{4}$ and $4d^{5}$ $5s^{1}$, respectively. The wave functions of valence electrons were expanded using a plane-wave basis set within a specified cutoff energy 720 eV. The convergence standards were set as 5×10^{-7} eV atom^{-1} for self-consistent field (SCF) tolerance, 0.01 eV Å^{-1} for maximum force, 5×10^{-4} Å for maximum displacement tolerances, 0.02 GPa for maximum stress and 5×10^{-6} eV atom^{-1} for total energy change in the geometry optimization. The Monkhorst-Pack scheme *k*-points grid sampling was set as $6 \times 6 \times 1$ for films structural optimization and properties calculations. The 2×2, 3×3 and 4×4 supercell was build to study the electronic properties of MoS$_2$ with one and two S vacancies on the surface, which was shown in Figure S1 (Supporting Information). The formation energy of S vacancy in the condition of with and without Na atom adsorpted on the MoS$_2$ surface as a function of temperature is followed by:

$$E_{f}^{slab+Na} = E_{MoS_2+Na}^{slab} - (E_{MoS_2-V_S}^{slab} + E_{Na}^{atom} + E_{s}^{atom}) \tag{2}$$

$$E_{f_{Vs}}^{slab+Na} = E_{MoS_2-V_S}^{slab} - (E_{MoS_2+Na}^{slab} - E_{Na}^{atom} - E_{s}^{atom}) \tag{3}$$

$$E_{f_{Vs}}^{slab} = E_{MoS_2-V_S}^{slab} - E_{MoS_2}^{slab} + E_{S}^{atom} \tag{4}$$

$$E_{S}^{atom} = E_{SO_2}^{gas} - E_{O_2}^{gas} \tag{5}$$

where $E_{f_{Vs}}^{slab+Na}/E_{f_{Vs}}^{slab}$ are the formation energy of Vs with/without Na atom absorbed on the MoS$_2$ surface, $E_{MoS_2+Na}^{slab}$ is the total energy of monolayer MoS$_2$with Na atom absorbed on the MoS$_2$ surface, E_{Na}^{atom}, E_{s}^{atom}, $E_{MoS_2}^{slab}$ and $E_{MoS_2-V_S}^{slab}$ are the total energies of Na, S atom, perfect MoS$_2$, and MoS$_2$ with one Vs on the surface, respectively, $E_{SO_2}^{gas}$ and $E_{O_2}^{gas}$ is the total energy of SO$_2$ and O$_2$.

Supporting Information

Supporting Information is available from the Wiley Online Library or from the author.

Acknowledgements

H.H. and F.T. contributed equally to this work. This work was supported by the“111” Project of China (D17017), the National Natural Science Foundation of China (62174015), the Developing Project of Science and Technology of Jilin Province (YDZJ202401368ZYTS).

Conflict of Interest

The authors declare no conflict of interest.

Data Availability Statement

The data that support the findings of this study are available from the corresponding author upon reasonable request.

Keywords

basal plane activation, defect engineering, monolayer MoS$_2$, NaCl, SERS

Received: June 8, 2024
Revised: August 23, 2024
Published online:

[1] Z. H. Zheng, S. Cong, W. B. Gong, J. N. Xuan, G. H. Li, W. B. Lu, F. X. Geng, Z. G. Zhao, *Nat. Commun.* **2017**, *8*, 1993.
[2] Y. R. Liu, Z. B. Gao, M. Chen, Y. Tan, F. Chen, *Adv. Funct. Mater.* **2018**, *28*, 1805710.
[3] M. W. Yu, S. Ishii, S. Li, C. J. Ku, S. Y. Chen, T. Nagao, K. P. Chen, *Appl. Surf. Sci.* **2022**, *605*, 154767.
[4] H. H. Sun, M. G. Yao, S. Liu, Y. P. Song, F. R. Shen, J. J. Dong, Z. Yao, B. Zhao, B. B. Liu, *ACS Appl. Mater. Interfaces* **2021**, *13*, 26551.
[5] W. J. Zhang, J. K. Huang, C. H. Chen, Y. H. Chang, Y. J. Cheng, L. J. Li, *Adv. Mater.* **2013**, *25*, 3456.
[6] C. Muehlethaler, C. R. Considine, V. Menon, W. C. Lin, Y. H. Lee, J. R. Lombardi, *ACS Photonics* **2016**, *3*, 1164.
[7] G. Song, W. B. Gong, S. Cong, Z. G. Zhao, *Angew. Chem., Int. Ed.* **2021**, *60*, 5505.
[8] P. Zuo, L. Jiang, X. Li, P. Ran, B. Li, A. S. Song, M. Y. Tian, T. B. Ma, B. S. Guo, L. T. Qu, Y. F. Lu, *Nanoscale* **2019**, *11*, 48.
[9] X. Wang, J. Wu, Y. W. Zhang, Y. Sun, K. K. Ma, Y. Xie, W. H. Zheng, Z. Tian, Z. Kang, Y. Zhang, *Adv. Mater.* **2022**, *35*, 2206576.
[10] S. Y. Sun, J. Y. Zheng, R. H. Sun, D. Wang, G. L. Sun, X. S. Zhang, H. Y. Gong, Y. Li, M. Gao, D. W. Li, G. C. Xu, X. Liang, *Nanomaterials-Basel* **2022**, *12*, 896.
[11] C. Wei, W. Z. Wu, H. Li, X. C. Lin, T. Wu, Y. D. Zhang, Q. Xu, L. P. Zhang, Y. H. Zhu, X. N. Yang, Z. Liu, Q. Xu, *ACS Appl. Mater. Interfaces* **2019**, *11*, 2526.
[12] Z. Y. He, R. Zhao, X. F. Chen, H. J. Chen, Y. M. Zhu, H. M. Su, S. X. Huang, J. M. Xue, J. F. Dai, S. Cheng, M. L. Liu, X. W. Wang, Y. Chen, *ACS Appl. Mater. Interfaces* **2018**, *10*, 42524.
[13] F. Bertoldo, R. R. Unocic, Y. C. Lin, X. H. Sang, A. A. Puretzky, Y. L. Yu, D. Miakota, C. M. Rouleau, J. Schou, K. S. Thygesen, D. B. Geohegan, S. Canulescu, *ACS Nano* **2021**, *15*, 2858.

[14] J. F. Xie, H. Zhang, S. Li, R. X. Wang, X. Sun, M. Zhou, J. F. Zhou, X. W. D. Lou, Y. Xie, *Adv. Mater.* **2013**, *25*, 5807.
[15] S. Santhoshkumar, W. S. Wei, M. Madhu, W. B. Tseng, W. L. Tseng, *J. Phys. Chem.* **2023**, *127*, 8803.
[16] H. Sharona, *J. Appl. Phys.* **2021**, *130*, 084303.
[17] Y. S. Huang, Y. T. Liu, T. P. Perng, M. Y. Lu, Y. L. Chueh, L. J. Chen, *Nano Energy* **2023**, *109*, 108295.
[18] P. K. Chow, R. B. Jacobs-Gedrim, J. Gao, T. M. Lu, B. Yu, H. Terrones, N. Koratkar, *ACS Nano* **2015**, *9*, 1520.
[19] W. G. Lu, B. Birmingham, Z. R. Zhang, *Appl. Surf. Sci.* **2020**, *532*, 147461.
[20] N. T. T. Vu, L. Loh, Y. Chen, Q. Y. Wu, I. A. Verzhbitskiy, K. Watanabe, T. Taniguchi, M. Bosman, Y. S. Ang, L. K. Ang, M. Trushin, G. Eda, *ACS Nano* **2023**, *17*, 15648.
[21] A. Singh, M. Moun, M. Sharma, A. Barman, A. K. Kapoor, R. Singh, *Appl. Surf. Sci.* **2021**, *538*, 148201.
[22] Y. R. Zhu, J. Lim, Z. P. Zhang, Y. Wang, S. Sarkar, H. Ramsden, Y. Li, H. Yan, D. Phuyal, N. Gauriot, A. Rao, R. L. Z. Hoye, G. Eda, M. Chhowalla, *ACS Nano* **2023**, *17*, 1354.
[23] S. S. Wang, Y. Rong, Y. Fan, M. Pacios, H. Bhaskaran, K. He, J. H. Warner, M. Pacios, *Chem. Mater.* **2014**, *26*, 6371.
[24] J. J. Ma, Z. X. Wang, B. Jiang, W. Wang, H. Wang, *Angew. Chem., Int. Ed.* **2023**, *62*, 202305846.
[25] K. Kaasbjerg, K. S. Thygesen, A. P. Jauho, *Phys. Rev. B* **2013**, *87*, 235312.
[26] G. Sharma, S. M. Rao, B. P. Singh, P. Vasa, *Appl. Phys. A* **2020**, *126*, 663.
[27] H. P. Komsa, S. Kurasch, O. Lehtinen, U. Kaiser, A. V. Krasheninnikov, *Phys. Rev. B* **2013**, *88*, 035301.
[28] W. H. Chae, J. D. Cain, E. D. Hanson, A. A. Murthy, V. P. Dravid, *Appl. Phys. Lett.* **2017**, *111*, 143106.
[29] J. Yang, Y. Wang, M. J. Lagos, V. Manichev, R. Fullon, X. J. Song, D. Voiry, S. Chakraborty, W. J. Zhang, P. E. Batson, L. Feldman, T. Gustafsson, M. Chhowalla, *ACS Nano* **2019**, *13*, 9958.
[30] S. S. Wu, T. X. Huang, X. L. Xu, Y. F. Bao, X. D. Pei, X. Yao, M. F. Cao, K. L. Lin, X. Wang, D. D. Wang, B. Ren, *ACS Nano* **2022**, *16*, 4786.
[31] D. C. Zhu, H. B. Shu, F. Jiang, D. H. Lv, V. Asokan, O. Omar, J. Yuan, Z. Zhang, C. H. Jin, *Npj 2D Mater. Appl.* **2017**, *1*, 8.
[32] H. W. Zhang, E. T. Poh, Y. M. Zhang, H. Y. Qin, H. N. Xie, C. N. He, S. Lim, C. H. Sow, *2D Mater.* **2023**, *10*, 035018.
[33] P. Man, S. Jiang, K. H. Leung, K. H. Lai, Z. Q. Guang, H. L. Chen, L. L. Huang, T. R. Chen, S. Gao, Y. K. Peng, C. S. Lee, Q. M. Deng, J. Zhao, T. H. Ly, *Adv. Mater.* **2023**, *36*, 2304808.
[34] J. R. Lombardi, R. L. Birke, *J. Phys. Chem. C* **2014**, *118*, 11120.
[35] K. Y. An, M. P. Chen, B. C. He, H. Pan, *Adv. Mater. Technol. -USA* **2022**, *7*, 2200217.
[36] X. Y. Hou, Q. Lin, Y. J. Wei, Q. H., Z. H. Ni, T. Qiu, *J. Phys. Chem. Lett.* **2020**, *11*, 7981.